SUPPLEMENTARY INFORMATION

Optical resonances of hollow nanocubes controlled with sub-particle structural morphologies

Jesus Valdez[1], Lucas V. Besteiro[1,2], Zakaria Mahfoud[1], Tugrul Guner[1] and Aycan Yurtsever[1]*

[1]*Centre Energie, Matériaux et Télécommunications, Institut National de la Recherche Scientifique (INRS), 1650 Boulevard Lionel-Boulet, Varennes, QC, J3X 1S2, Canada*

[2] *Institute of Fundamental and Frontier Sciences, University of Electronic Science and Technology of China, Chengdu 610054, China*

Corresponding author:

* E-mail: yurtsever@emt.inrs.ca

Supplementary information I

The UV-vis-NIR was used to analyze the absorbance of all the samples of both templates, including the AgNCs. Figure S1 shows all the absorbance spectra for all the 12 samples of hollow-MNP (6 samples per each template), in which is noticeable the red shifting of the plasmonic absorptions from the AgNCs templates (black) to the hollow-MNPs by using different additions of $HAuCl_4$.

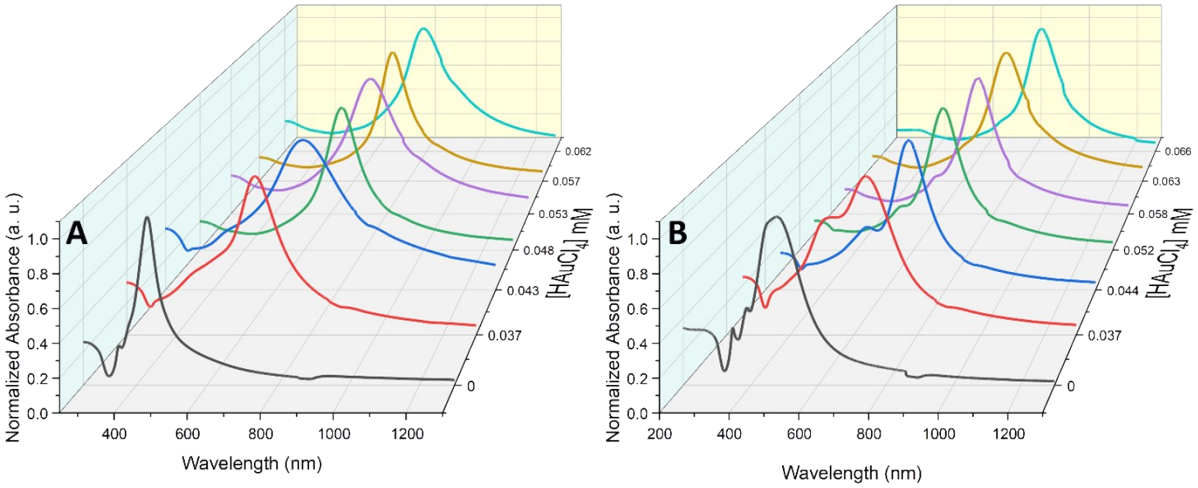

Figure S1. Absorbance spectra of AgNCs (black) and hollow-MNPs for the a) small and b) large templates at different concentractions of $HAuCl_4$.

Supplementary information II

We performed extensive SEM and ADF-STEM characterization for all the 12 samples we synthesized. Figures S2 and S3 show SEM and ADF-STEM images of hollow-MNPs for every step of the galvanic replacement process. In these images, the evolution of the voids and pinholes is evident.

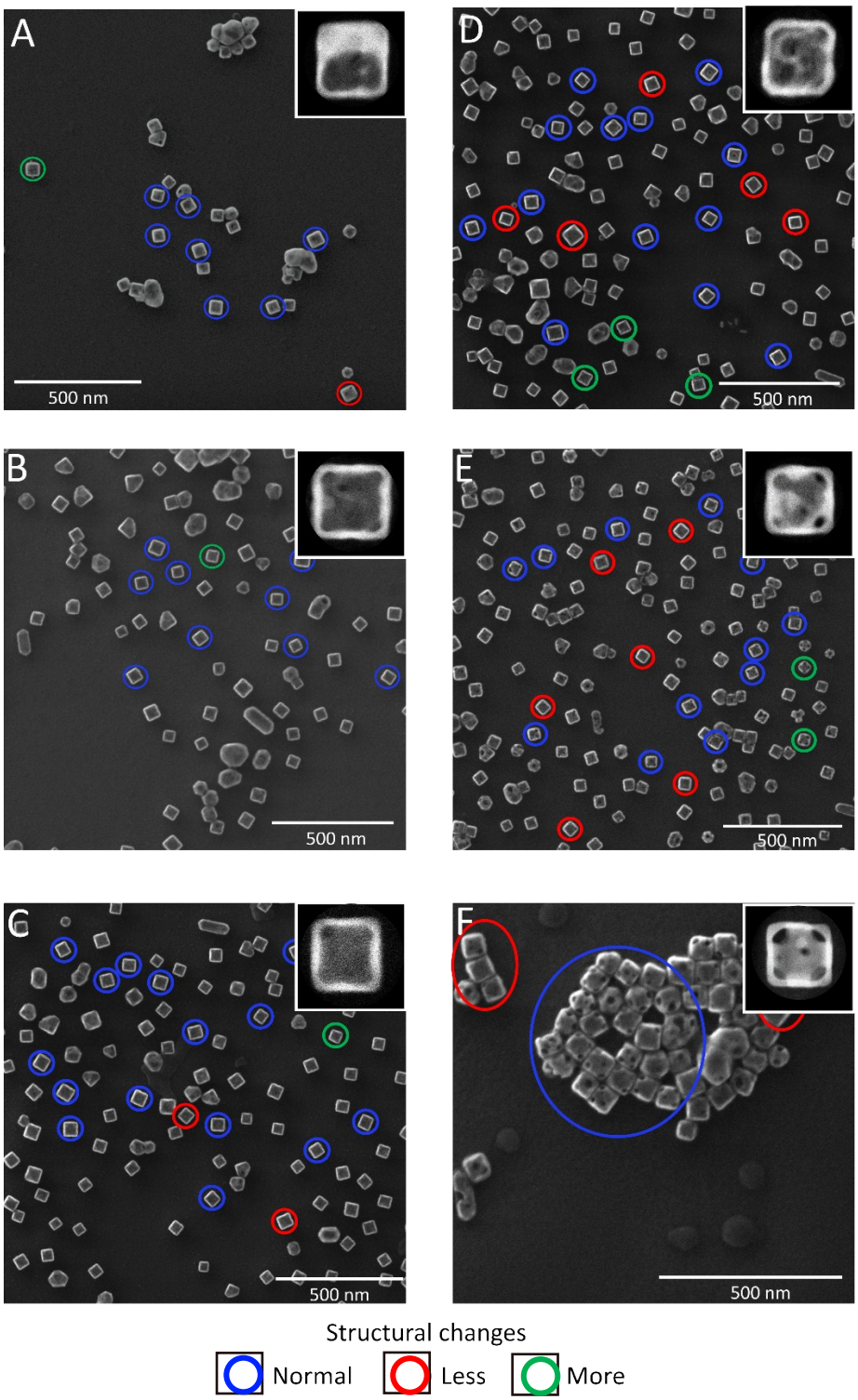

Figure S2. SEM images of hollow-MNPs for the small template. $HAuCl_4$ concentration increases from A to F. The inset shows the ADF- STEM image for a single nanoparticle showing the characteristic structural features of the ensemble.

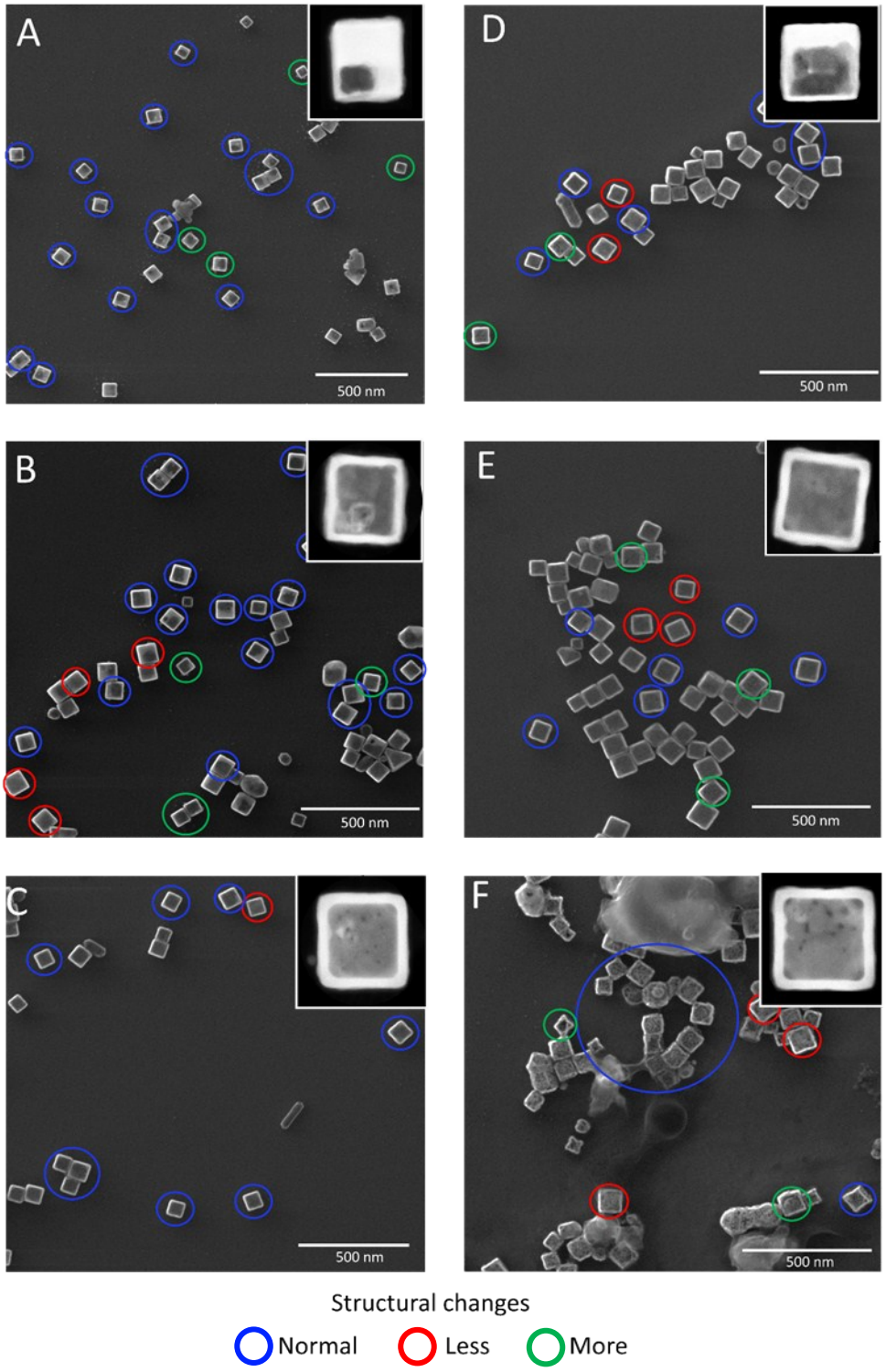

Figure S3. SEM images of hollow-MNPs for the small template. $HAuCl_4$ concentration increases from A to F. The inset shows the ADF-STEM image for a single nanoparticle showing the characteristic structural features of the ensemble.

Supplementary information III

The statistical analysis of hollow-MNPs was performed with an automated code that can effectively measure the wall thicknesses and total sizes of all the particles in an SEM image. Figure S4 shows the histograms of wall thickness and total sizes of hollow-MNPs. This information was used to get the internal and outer wall thicknesses. The histograms represent the analysis of 100 nanoparticles for each sample.

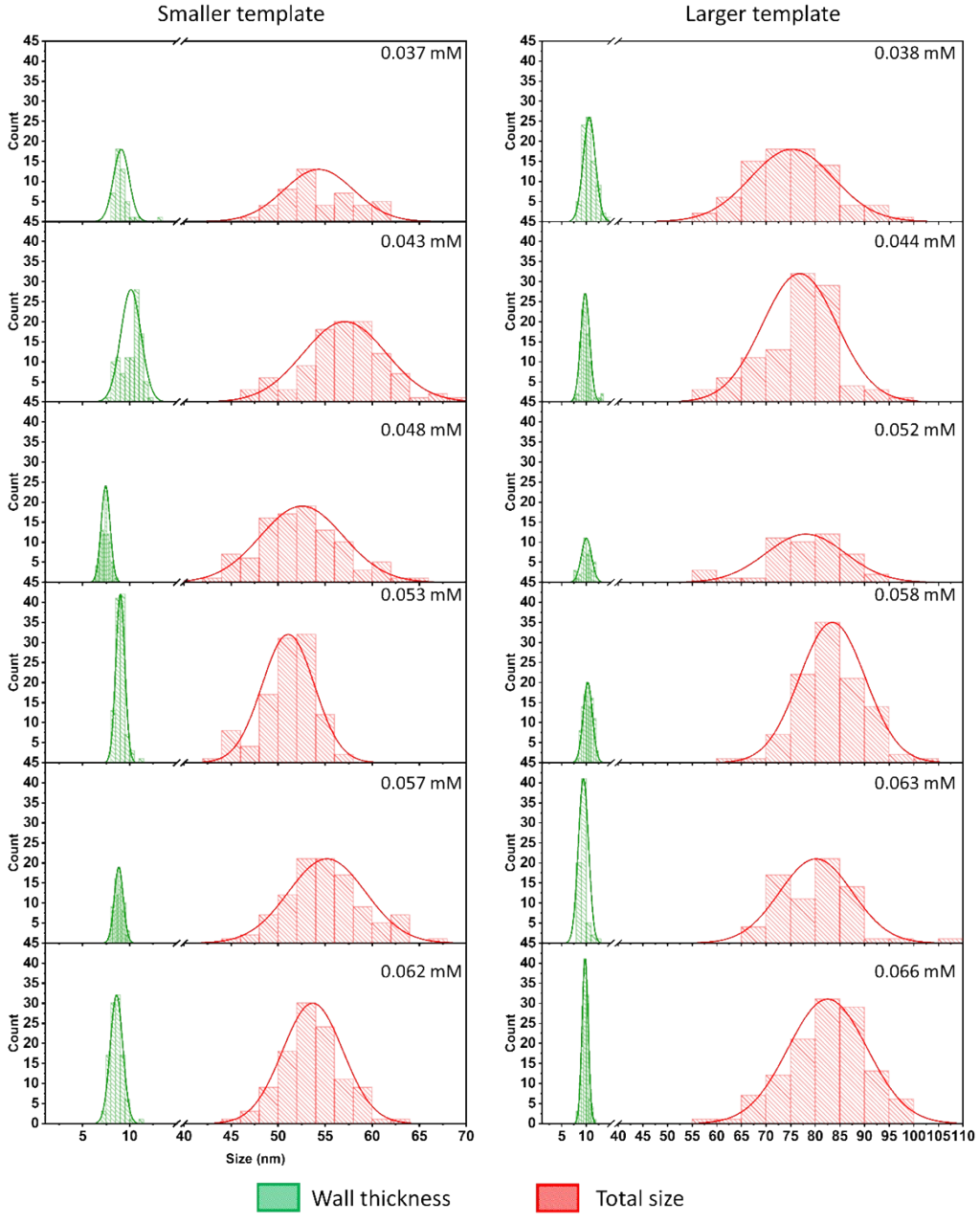

Figure S4. Statistical dimensionality analysis for the small and large hollow-MNP. The total size distributions of the hollow-MNPs (red) and distributions of their wall thicknesses (green) are shown.

Supplementary information IV

We have captured HR-TEM images of representative samples, which were synthesized by employing different reaction conditions depending on the use of small or large template and also depending on the concentration of $HAuCl_4$ and presented in Figure S5. Images of hollow-MNPs demonstrate the effect of galvanic replacement process including both small and large templates on their structure. In these images, the evolution of the voids and pinholes are evident as it was observed already in SEM and STEM images presented in Figure S2 and S3.

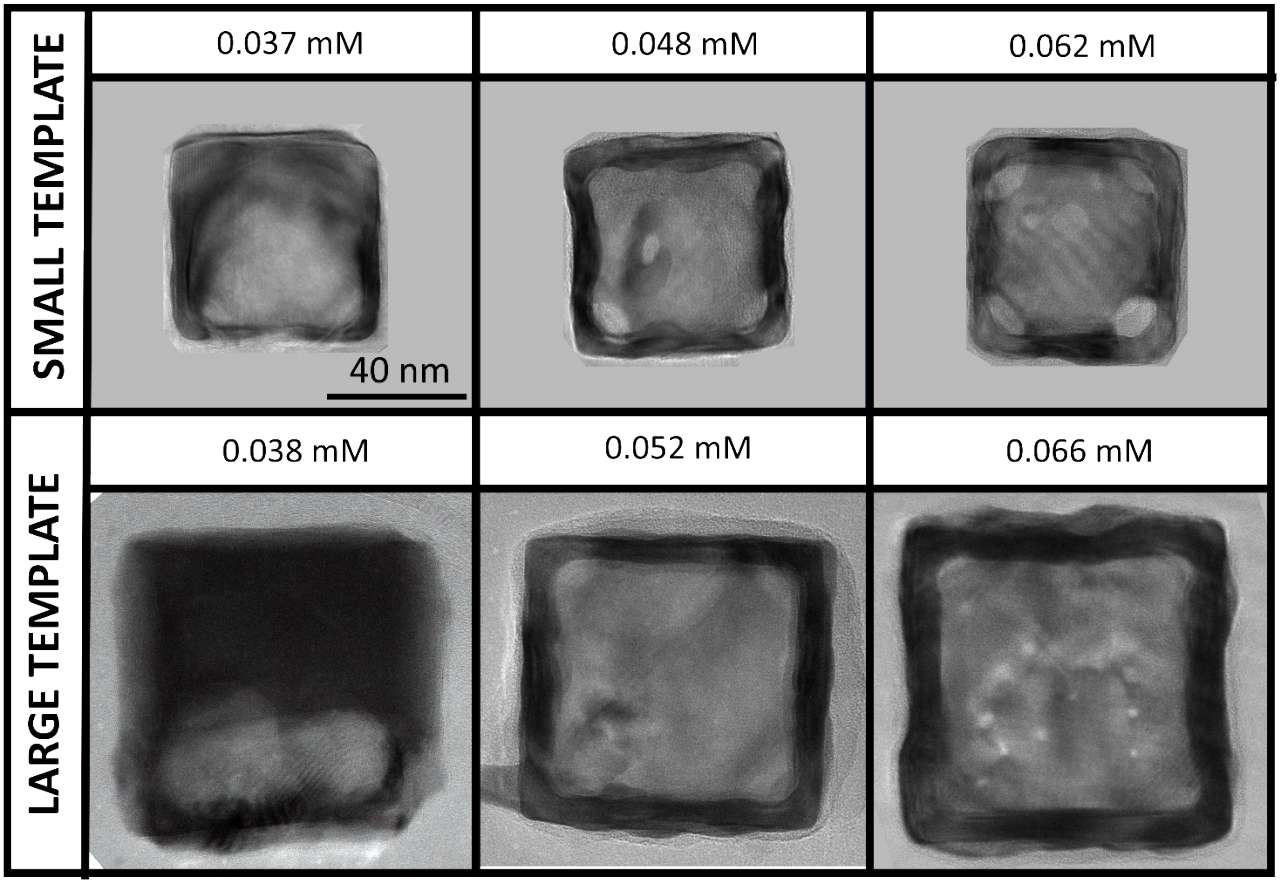

Figure S5. HR-TEM images of hollow-MNPs for the small and large templates depending on the $HAuCl_4$ concentration, which increases from left to right.

Supplementary information V

The main text features a discussion on the coupling of the plasmonic modes associated with the inner and outer surfaces in the MNPs. Figures S6 and S7 below shows detailed data for the three irreducible light polarizations for the MNPs with a void height of 20 nm (panel a), in comparison with the equivalent geometry with a fully developed void (panel b). Together, panels a and b illustrate the impact of the geometrical asymmetry over the optical spectra.

The difference between Figures S6 and S7 is the degree of coupling between particle and cavity plasmonic modes, modeled through the MNP wall thickness. Figure S5 shows results obtained from the geometry with wall thickness equal to the mean experimental value (See table T2), while Figure S7 uses half of these values.

Panels an in both these figures complement the discussion around Figure 4b in the main text. Here we see the spectra of each independent light polarization, and we can better identify the interaction between specific modes and how do they relate to the broken cube symmetry of the model's geometry. Particularly, we see the clear difference between the spectra under light polarized along the *y* and *z* directions in Figure S6a. The equivalent difference is not as appreciable in the weak coupling regime, i.e., Figure S6a, which is, of course, part of the reason why this geometry did not produce the shoulder in the average data depicted in Figure 4b in the main text. The other factor is that for the thicker wall data (Figure S6), the coupling is not strong enough to hybridize the outer and inner modes. The high-energy cavity modes in Figure S6 can be seen in the absorption cross sections (or through monitoring the quadrupole component of the multipolar expansion of the charge distribution), but this is not enough to appreciably change the global extinction spectrum. This changes when the coupling becomes strengthened (Figure S7a) and the hybridization of the modes separate them in energy and changes their spatial symmetry, converting both high- and low- energy resonances in bright modes that noticeably contribute to the global extinction cross-section of the MNP.

Comparing panels b from Figures S6 and S7 straightforwardly evidences the effect of the increased coupling. The main plasmonic peak becomes strongly redshifted upon reducing the wall thickness (increasing coupling strength), and so does the secondary peak as additional higher-order modes appear at higher frequencies.

Lastly, Figure S8 illustrates a similar phenomenon, occurring in the MNPs with open features at their surfaces, which explains the continuing redshift when increasing Au concentration after reaching the point of full void development. In this case, it is the additional high-frequency hole plasmonic modes that interact with the main full-particle excitation and thus drive the redshift in the last set of datapoint in Figure 5 in the main text. Interestingly, we can see that these high-frequency modes are dark modes and their scattering cross section is negligible.

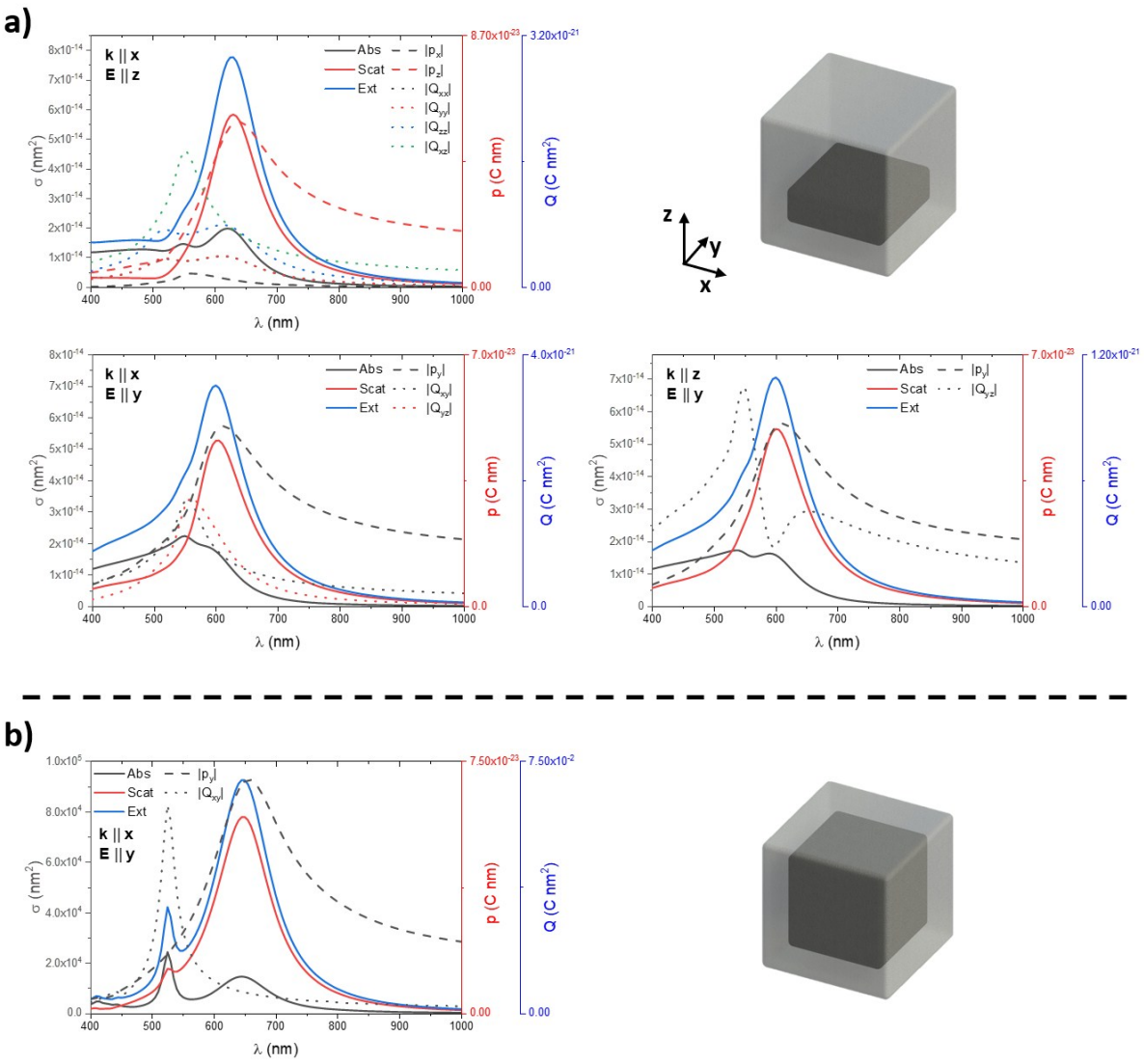

Figure S6. **Weak coupling.** Optical cross sections (σ) and dominant dipolar (p) and quadripolar (Q) moments of the charge distribution in the particle with a 55x55x20 nm void (panel a) and a 55x55x55 nm void (panel b). Thus, they correspond to geometrical models with wall thicknesses equal as presented in tables T1 and T2.

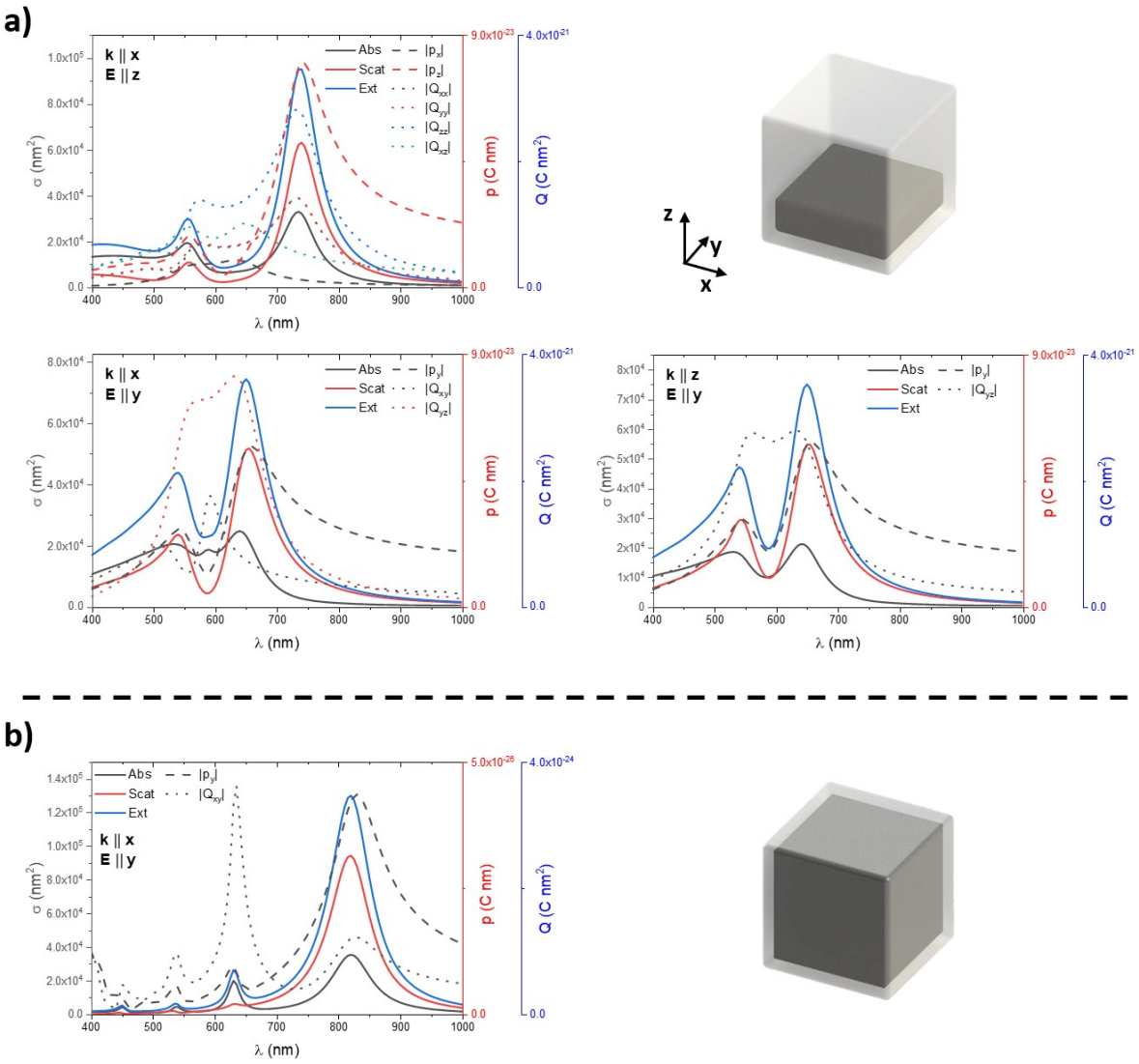

Figure S7. **Strong coupling**. Optical cross sections (σ) and dominant dipolar (p) and quadripolar (Q) moments of the charge distribution in the particle with a 65x65x20 nm void (panel a) and a 65x65x65 nm void (panel b). Thus, they correspond to geometrical models with wall thicknesses equal to half the values presented in tables T1 and T2.

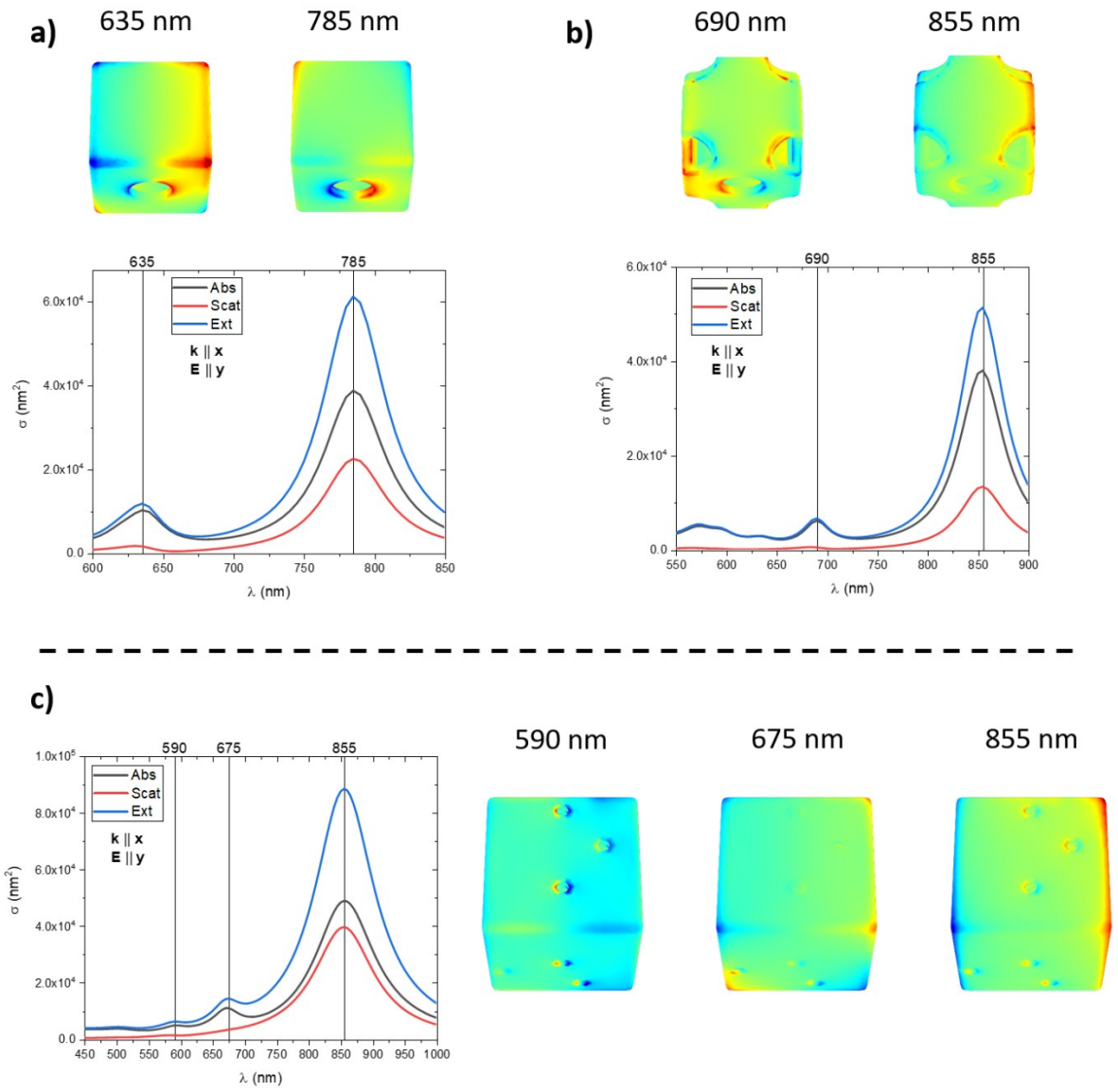

Figure S8. **Strong coupling**. Interaction cross sections σ and surface charges for MNPs with wall thickness equal to one half the values presented in tables T1 and T2, showing the strong-coupling regime between the charges at the outer and inner MNPs' surfaces. We showcase results for specific light incidences, illustrating the spatial symmetry of the main plasmonic modes. The data has been chosen from representative geometries with fully developed voids and hollow surface features. a) Small template, single pinhole. b) Small template, single pinhole, eight truncated holes. c) Large template, three pinholes per face.